


## Controlled collision of Hele-Shaw drops in extensional flow using a six-port microfluidic device

Aysan Razzaghi  and Arun Ramachandran\**Faculty of Applied Science & Engineering, University of Toronto, 200 College Street, Toronto, Ontario, Canada M5S 3E5*

(Received 6 July 2022; accepted 1 August 2023; published 28 August 2023)

Collision of two dispersed drops in the matrix of a suspending liquid is the first step toward coalescence. However, to quantify the rate of coalescence, the configuration of the collision should be definable and the force that induces the collision should be measurable. We present a strategy to use the hydrodynamic force in a six-port microfluidic channel to steer two drops toward collision in extensional flow. By implementing the analytical solution in the control loop, the flow rates that are required to steer the drops toward their respective target points can be determined using a single control parameter. This parameter,  $\chi^*$ , is a dimensionless timescale that can manipulate the drops in two limits: (1) by engaging all six ports to create a flow field with two stagnation points ( $\chi^* \ll 1$ ), or (2) by deactivating some of the ports and creating a linear extensional flow through the remaining active ports ( $\chi^* \gg 1$ ). We determine specific orientations that are more suitable for the collision of Hele-Shaw drops in the six-port microfluidic channel. Based on the above strategy, we design and perform controlled head-on and glancing collisions for  $\sim 100 \mu\text{m}$  radius Hele-Shaw perfluorodecalin drops in silicone oil. Using the conformal mapping technique, the analytical solution of the flow field accounting for the perturbation of the flow due to the hydrodynamic interactions between the Hele-Shaw drops was used in the control code. Coalescence time between two Hele-Shaw drops undergoing a head-on collision in a dimpled mode was found to be independent of the strain rate of the hydrodynamic flow.

DOI: [10.1103/PhysRevFluids.8.084201](https://doi.org/10.1103/PhysRevFluids.8.084201)

### I. INTRODUCTION

Microfluidics has been integrated with external force fields such as magnetic, electric, acoustic, and optical fields to perform manipulation, deformation, adhesion, and separation of soft particles and biological cells [1–8]. Unfortunately, aside from the burden of setting up an external field in the experiments, the use of these external fields is subjected to limitations on particle and material type. For instance, the use of magnetic controllers is only limited to magnetic particles [5]. Optical forces can cause heating issues which may alter the local viscosity [9]. Also, the electric and the acoustic forces exert an inordinate stress that can damage the delicate biological cells [10]. These problems associated with external fields prompt the question—can the flow field naturally available on the microfluidic platform—the hydrodynamic field—be used to manipulate particles? The answer to this question, as has been shown in several recent studies [11–21], is an overwhelming “yes.” In these studies, which are inspired by the four-roll mill [11–13,22], isolation and manipulation of a single micron size particle or drop was demonstrated. The trapped particle or drop experienced a measurable hydrodynamic force from the flow by showing deformation, which was used to assess

\*Corresponding author: [arun.ramchandran@utoronto.ca](mailto:arun.ramchandran@utoronto.ca)

the rheological properties of the interface such as interfacial tension [14,20,21,23–25]. Two-drop coalescence experiments were also performed by Leal and co-workers [26–31], but Shenoy *et al.* [32], inspired by Schneider *et al.* [17], recently took this to the microfluidic level by confining and manipulating two particles with six, evenly distributed side channels along a hexagonal microfluidic chamber [32,33]. Model predictive control (MPC) was implemented as a control code to enhance the stability of control. The flow-induced interaction and adhesion of two suspended particles from 0.1  $\mu\text{m}$  Brownian particles to 10  $\mu\text{m}$  noncolloidal particles was demonstrated using such device [32,33]. In a recent study, Boyd *et al.* [34] designed a dual microfluidic trap by interconnecting two cross-slot extensional hydrodynamic traps and employing a proportional feedback control algorithm. Simultaneous confinement of two particles (up to 10  $\mu\text{m}$ ) placed at the stagnation point of each cross-slot trap has been achieved by tuning the strain rate at either trap. Although the dual hydrodynamic trap allows for limited adjustment of interparticle distance, collision and adhesion of particles is experimentally more cumbersome.

We [35] and others [36] have adapted the six-port microfluidic device to the flow of drops. The analytical [27,35] code, in which the streamline velocity in the absence of drops is assumed to be proportional to the current and target points, and the MPC code [36], exerted control over the motion of the drops in a precise manner, and collision leading to coalescence was also observed. The systems examined were light mineral oil as the suspending medium and water as the drop medium, with Span 80 in the oil phase as surfactant [35,36].

In this paper, we introduce two ideas to the manipulation and control of a pair of drops. First, the analytical code, which functions on matrix inversion to yield flow rates [13], has received little attention [34]. The analytical code was deemed impractical for experiments because of unrealistically large flow rates associated with the close encounter of two particles. Instead, the MPC code was used, which optimizes and moderates the fluxes to create the flow. However, as we shall show in the next section, the analytical code uses a single parameter—the flow rate through one of the ports—to determine the flow rates through the remaining ports. Using a single dimensionless parameter  $\chi^*$  based on this flow rate, we are able to send the drops to their respective target points either by placing the stagnation points near the drops involving all six of the ports ( $\chi^* \ll 1$ ), or by deactivating one port so that we are reduced to a five-port flow ( $\chi^* \gg 1$ ). Hence, we can trap the drops in the limit  $\chi^* \ll 1$ , and perform head-on or glancing collision created by the linear extensional flow in the limit  $\chi^* \gg 1$ . It is similar in concept to the papers mentioned above [32,33], but much simpler in execution by the switch of a button. The advantage of this method is that drops always tend to move along the straight line connecting the initial and target positions at a user-prescribed speed. Using this idea, we outline the manner in which head-on and glancing collision can be done. Second, we use not spherical drops but Hele-Shaw drops (the reason is explained in Sec. III). We use a simple theory to achieve precise control over the soft Hele-Shaw particles by using a first-order correction to Stokes flow without compromising on the speed of control. When a Hele-Shaw drop moves with a certain velocity in a linear flow, the far field disturbance decays quadratically with distance [37–41], and in an extensional flow, it decays cubically with distance [42]. Therefore, at the limit of  $\chi^* \ll 1$  where each drop is confined to the stagnation point of the local extensional flow, the disturbance decays cubically. On the other hand, for  $\chi^* \gg 1$  the disturbance is mediated quadratically with distance. So, if two drops are separated only by a few drop radii, hydrodynamic interactions by the method of reflections become important, and control strategies based on point-particle solutions can fail [42]. In particular, we perform a head-on collision between similarly sized Hele-Shaw drops at a variety of capillary numbers in the dimpled state, and generate a capillary number coalescence time curve. Interestingly, in the dimpled regime, the coalescence time is independent of the capillary number.

The article is organized as follows. Section II sets out the theory of the control algorithm. Section II A explains the principles of the matrix inversion method for the point-particles solution, defines the control parameter  $\chi^*$ , and demonstrates the effects of  $\chi^*$  on the flow topology. Section II B presents strategies to induce head-on and glancing collisions in the linear extensional flow generated in the six-port microfluidic extensional flow device (MEFD). Section II C discusses the range within

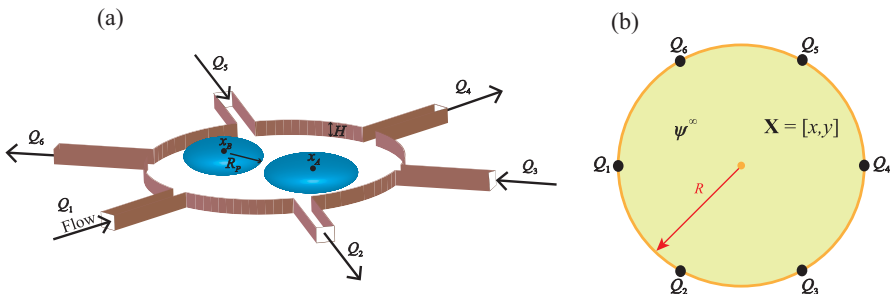


FIG. 1. (a) Schematic of the six-port MEFD with two channel-spanning soft particles. Here, we have shown Hele-Shaw particles, where the radius of the particles,  $R_p$ , is greater than the channel depth,  $H$ , so that the particles adopt the shape of a pancake. But, particles smaller than the depth can be controlled as well (see Sec. III). The flow of the fluid through the side channels leads to the creation of the flow field inside the circular main channel. (b) Geometry of the six-port MEFD circle and the flow field ( $\psi^\infty$ ) developed for the point objects.

which the value of  $\chi^*$  can be tuned. Section III discusses the reason for employing Hele-Shaw drops in this study and applies leading-order correction to the flow field used in Sec. II A to capture the effects of the flow disturbance due to the presence of Hele-Shaw drops. Section IV deals with the experimental methods and procedure, and Sec. V discusses the results of experiments. Section V A demonstrates accuracy and speed of the control for a pair of Hele-Shaw drops. Section V B presents the experimental results of head-on and glancing collision. Section V C compares the experimental drainage time of collision with the theoretically derived drainage time. A discussion of analytical method and other details in Sec. VI follows suit. Section VII ends with the conclusions and future work.

## II. THE CONTROL ALGORITHM

### A. Principles of the algorithm

The six-port microfluidic extensional flow device (MEFD) [Fig. 1(a)] consists of a circular main channel of radius  $R$  and depth  $H$ , with six evenly distributed side channels to allow the fluid to flow in and out, thus creating a steady flow. The analytical solution of the flow field in depth-averaged coordinates,  $\mathbf{v}^\infty(\mathbf{x}, \mathbf{Q}/H)$ , is already known for point objects inside the six-port MEFD [17,32,35] and is determined by solving the Laplace equation for the stream function  $\psi^\infty$ , with appropriate boundary conditions at the six circular arcs of the boundary based on the flow rate vector  $\mathbf{Q} = [Q_1, Q_2, \dots, Q_6]$  [Fig. 1(b)]. The velocity field is assumed to be steady and instantaneously responsive to changes in the flow rate. ‘‘Point’’ particles are simply advanced in time by the velocity field,  $\mathbf{v}^\infty = [\frac{\partial \psi^\infty}{\partial y}, -\frac{\partial \psi^\infty}{\partial x}]$ , predicted by this solution (we only consider convection; Brownian motion is ignored [34]). Consider, for example, two point particles,  $A$  and  $B$ , at positions  $\mathbf{x}_A$  and  $\mathbf{x}_B$  in the main channel’s circle. The flow rates in the side channels ( $\mathbf{Q}$ ) should be adjusted such that the instantaneous particle velocities steer the particles from their current positions toward the target points ( $\mathbf{x}_{A_T}$  and  $\mathbf{x}_{B_T}$ , respectively), i.e.,

$$\mathbf{v}_P^\infty(\mathbf{x}_A, \mathbf{x}_B, \mathbf{Q}/H) = \chi_A(\mathbf{x}_{A_T} - \mathbf{x}_A), \quad (1a)$$

and

$$\mathbf{v}_P^\infty(\mathbf{x}_B, \mathbf{x}_A, \mathbf{Q}/H) = \chi_B(\mathbf{x}_{B_T} - \mathbf{x}_B), \quad (1b)$$

where  $\chi_A$  and  $\chi_B$  in  $s^{-1}$  are the gain parameters. Substituting for the velocity  $\mathbf{v}_p^\infty$  from the Supplemental Material [43] (which also contains Refs. [44–48]), Sec. A [44], we have

$$\mathbf{A} [Q_1 \ Q_2 \ Q_3 \ Q_4 \ Q_5]^T = \begin{bmatrix} \chi_A (\mathbf{x}_{A_T} - \mathbf{x}_A) \\ \chi_B (\mathbf{x}_{B_T} - \mathbf{x}_B) \end{bmatrix}. \quad (2)$$

Here,  $\mathbf{A}$ , having units of  $1/m^2$ , is a  $4 \times 5$  matrix that gives the velocity when multiplied with the flow rates. There are six flow rates, but since the conservation of mass requires  $\sum_{m=1}^6 Q_m = 0$ , there are really only five unknown flow rates. This is a vector set of four equations that is linear in the flow rate vector,  $\mathbf{Q}$ . Thus, as also noted by Schneider *et al.* [17], Shenoy *et al.* [32], and Kumar *et al.* [35], there is an extra degree of freedom. This can be exploited to impose other constraints, but in this work, we tune the control by writing

$$\mathbf{A}' [Q_2 \ Q_3 \ Q_4 \ Q_5]^T = \chi \begin{bmatrix} \mathbf{x}_{A_T} - \mathbf{x}_A \\ \mathbf{x}_{B_T} - \mathbf{x}_B \end{bmatrix} + Q_1 \mathbf{B}', \quad (3)$$

where  $\mathbf{A}'$  is a  $4 \times 4$  matrix, and  $\mathbf{B}'$  is a  $4 \times 1$  vector. In this work, for ease of implementation, we have taken  $\chi_A = \chi_B = \chi$ ; an example of  $\chi_A \neq \chi_B$  will be given later. Rendering the equation dimensionless, we have

$$\mathbf{A}^* \mathbf{Q}^* = \chi^* \begin{bmatrix} \mathbf{x}_{A_T}^* - \mathbf{x}_A^* \\ \mathbf{x}_{B_T}^* - \mathbf{x}_B^* \end{bmatrix} + \mathbf{B}^*, \quad (4)$$

where  $\mathbf{A}^*$  and  $\mathbf{B}^*$  are dimensionless versions of  $\mathbf{A}'$  and  $\mathbf{B}'$ , respectively,  $\mathbf{Q}^* = [Q_2 \ Q_3 \ Q_4 \ Q_5]^T / Q_1$ ,  $\mathbf{x}$  has been nondimensionalized by  $R$ , and  $\chi^*$  is

$$\chi^* = \frac{\chi R^2 H}{Q_1}. \quad (5)$$

$\chi^*$  is the characteristic timescale,  $R^2 H / Q_1$ , required to sweep the volume of the MEFD circle relative to the timescale of control,  $1/\chi$ .  $\chi^*$  has a major role to play in the control process. If  $\chi^* \ll 1$ , the first term in the right hand-side of Eq. (4) becomes negligible and  $\chi^*$  does not feature in the leading order in flow rate. In fact, for  $\chi^* = 0$ , as evident from Eq. (2), the flow matrix solution is a zero-eigenvalue problem. The only solution to the problem is that the velocity of the particles is zero [ $\mathbf{v}_p^\infty(\mathbf{x}_A, \mathbf{x}_B, R_B, \mathbf{Q}/H) = \mathbf{v}_p^\infty(\mathbf{x}_B, \mathbf{x}_A, R_A, \mathbf{Q}/H) = 0$ ]; i.e., the particles are put in their stagnation points, the point at which the flow speed is zero. Therefore, for  $\chi^* \ll 1$ , particles are only displaced marginally with respect to their stagnation points. For example, we often catch two particles in the configuration shown in Fig. 2 (the procedure for this initial trapping is described later in Sec. IV); the two particles are mirror images of each other. Now, in the simulation, each particle has a target location of the other particle ( $\mathbf{x}_{A_T}^* = \mathbf{x}_B^*$ , and  $\mathbf{x}_{B_T}^* = \mathbf{x}_A^*$ ) for simplicity; the particles are chasing each other. The  $Q_1$  port is always shown at  $180^\circ$  [Fig. 1(a)]. When the parameter  $\chi^*$  is zero, the particles occupy the stagnation points (shown with the letter S), as can be seen in Fig. 2(a). In Fig. 2(b), for  $\chi^* \ll 1$ , two stagnation points form adjacent to the position of the particles, driving the particles toward each other. All six side channels are engaged in creating the flow field in Figs. 2(a) and 2(b) in this configuration.

When  $\chi^* \gg 1$ ,  $\mathbf{B}^*$  becomes negligible, and the dimensionless flow rates  $[Q_2 \ Q_3 \ Q_4 \ Q_5]^T / Q_1$  scale linearly with  $\chi^*$  [Eq. (4)], and some of them increase dramatically with  $\chi^*$ . In fact,  $[Q_2 \ Q_3 \ Q_4 \ Q_5]^T$  scale linearly with the dimensional value of  $\chi$ ;  $Q_1$  is an inactive port [Eq. (3)]. Hence, the job of governing flow rates lies with five ports instead of six; the extra degree of freedom is lost. The loss of the  $Q_1$  port happens in the manner in Fig. 2. At  $\chi^* = 0.1$  [Fig. 2(b)], the stagnation point toward the  $240^\circ$  particle [Figure 1(b)] moves to the corner, and at  $\chi^* = 0.3$  [Fig. 2(c)] it merges with the boundary circle. At  $\chi^* = 1$  [Fig. 2(d)], the stagnation point on the circle splits into half stagnation points (shown with S'), as shown in the edge. At this point, flow in the two side channels,  $Q_1$ , due to restriction of the normalizing port, and  $Q_3$ , due to a symmetry

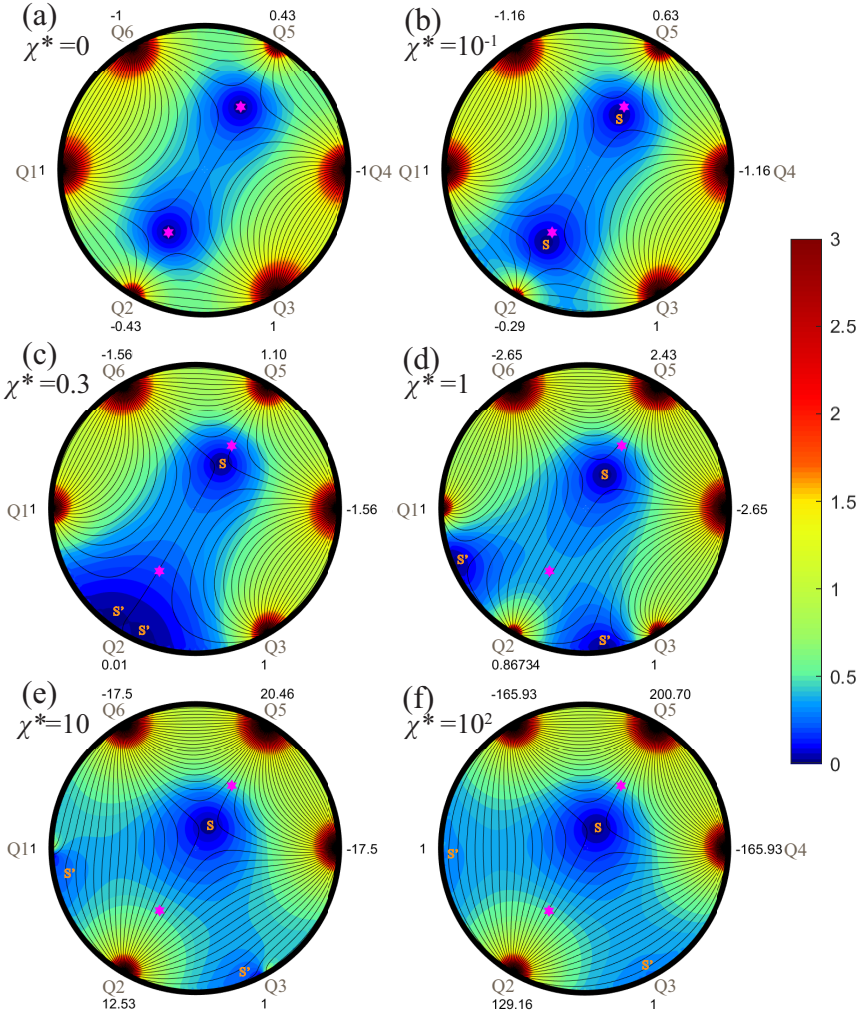


FIG. 2. Velocity contour and streamlines for two particles in the  $60^\circ$ – $240^\circ$  orientation (shown in magenta hexagrams) that are set to move toward each other at (a)  $\chi^* = 0$ , (b)  $\chi^* = 10^{-1}$ , (c)  $\chi^* = 0.3$ , (d)  $\chi^* = 1$ , (e)  $\chi^* = 10$ , and (f)  $\chi^* = 10^2$ . The stagnation points are shown with S and the half stagnation points in (c–f) are shown with S'.

requirement, become weaker. As  $\chi^* \gg 1$  [Figs 2(e) and 2(f)], two half stagnation points and a single full stagnation point form in the circular main channel. Two of the side channels,  $Q_1$  and  $Q_3$ , become completely inactive, and the flow field due to the remaining ports represents a four-port flow field. Note that, in the limit  $\chi^* \gg 1$ , with  $Q_1$  not active, there are usually five ports, but there are only four ports in Fig. 2(f) due to a mirror image.

The flow field in Fig. 2(f) for  $\chi^* \gg 1$  resembles the linear extensional flow between the two particles. It is created in between the two particles, and the line between the two also represents the converging flow of the linear field. The  $240^\circ$  particle is pulled toward the linear field by the two half stagnation points, and the  $60^\circ$  [Fig. 1(b)] particle is drawn toward the linear field by the full stagnation point. Thus, once the particles are in the respective positions (e.g., Fig. 2), just by switching to  $\chi^* \gg 1$ , one can create a head-on collision.



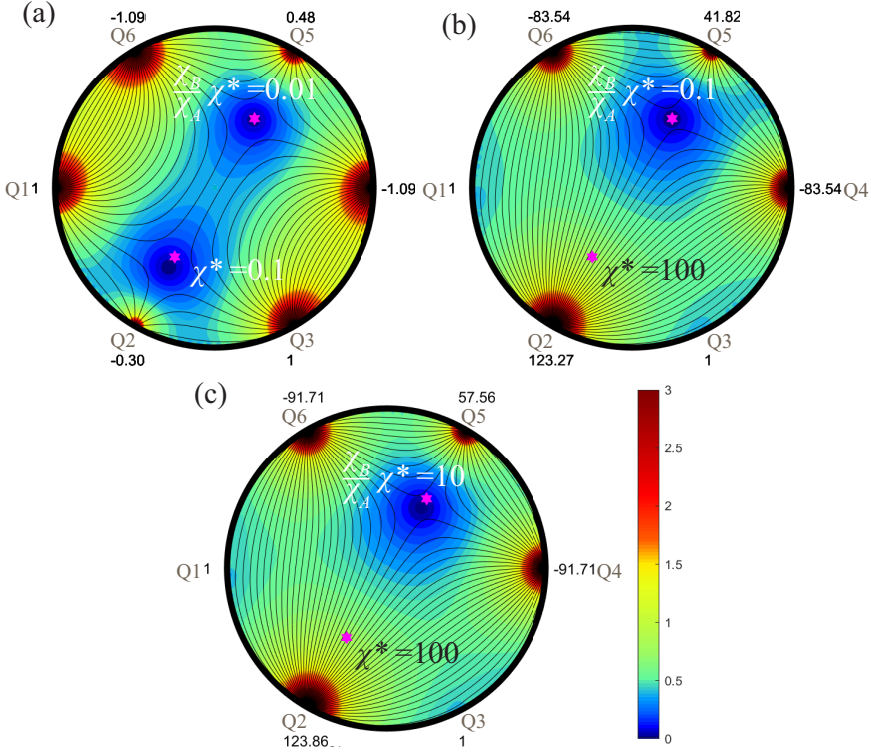


FIG. 3. Velocity contour and streamlines for two particles in the  $60^\circ$ – $240^\circ$  orientation (shown in magenta hexagrams) that are set to move toward each other with different  $\chi^*$  values. Assuming that  $\frac{\chi_B}{\chi_A} < 1$ , at (a)  $\chi_A^* = 0.1$  and  $\chi_B^* = 0.01$ , (b)  $\chi_A^* = 100$  and  $\chi_B^* = 0.1$ , and (c)  $\chi_A^* = 100$  and  $\chi_B^* = 10$ .

Two particles can be set to advance with two different  $\chi^*$  values as well. This is shown in Fig. 3, with an example that mimics Fig. 2, but with  $\chi_A$  and  $\chi_B < \chi_A$ , respectively [Eq. (2)]. In this case, the particles behave in the way according to Table I.

The  $\frac{\chi_B}{\chi_A} \chi^* \ll \chi^* \ll 1$  is similar to the  $\chi^* = 0.1$  case in Fig. 2(b) as it houses particles at their stagnation points. The case of interest is  $\frac{\chi_B}{\chi_A} \chi^* \ll 1 \ll \chi^*$ , where the particle at  $240^\circ$  is controlled by two half stagnation points, while the particle at  $60^\circ$  resides at a full stagnation point. This way, the particle at  $60^\circ$  can be stationary, while the particle at  $240^\circ$  comes and performs a head-on collision. Surprisingly, the flow pattern in  $1 \ll \frac{\chi_B}{\chi_A} \chi^* \ll \chi^*$  is more similar to that in  $\frac{\chi_B}{\chi_A} \chi^* \ll 1 \ll \chi^*$ . This implies that for the case of  $\chi_A \neq \chi_B$ , as long as  $\chi^* \gg 1$ , the flow pattern resembles Figs. 3(b) and 3(c). From here onwards, we shall proceed with  $\chi_A = \chi_B$ .

TABLE I. The behavior of the particles controlled by two different  $\chi^*$  values. Note that  $\chi_B$  is smaller than  $\chi_A$ .

Parameters	Results
$\frac{\chi_B}{\chi_A} \chi^* \ll \chi^* \ll 1$	Both particles will remain close to their stagnation points [Fig. 3(a)].
$\frac{\chi_B}{\chi_A} \chi^* \ll 1 \ll \chi^*$	Particle at $240^\circ$ enters the half stagnation point zone, while particle at $60^\circ$ will remain close to a stagnation point [Fig. 3(b)].
$1 \ll \frac{\chi_B}{\chi_A} \chi^* \ll \chi^*$	Particle at $240^\circ$ remains in the half stagnation zone, while particle at $60^\circ$ shows minor displacement from its full stagnation point [Fig. 3(c)].

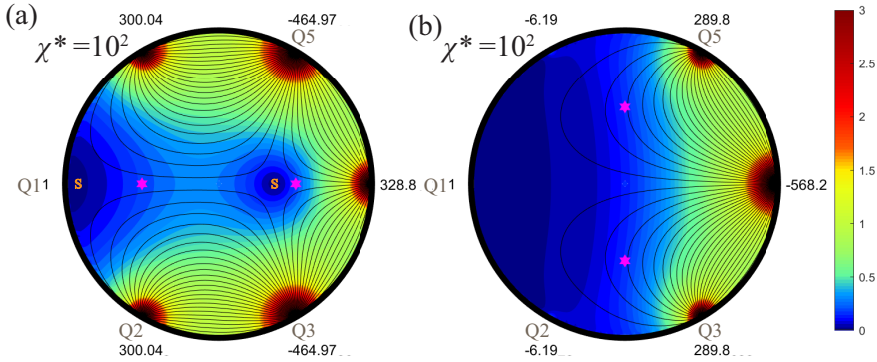


FIG. 4. Velocity contour and streamlines for two particles (shown in magenta hexagrams) that are set to move toward each other with  $\chi^* = 10^2$  (a) in the  $0^\circ$ – $180^\circ$  orientation and (b) in the  $90^\circ$ – $270^\circ$  orientation. The stagnation points are shown with S.

Let us now move to different orientations of the particles relative to the  $Q_1$  port. We had chosen the particles at angles of  $60^\circ$ – $240^\circ$  in Fig. 2. The  $120^\circ$ – $300^\circ$  orientation is identical to Fig. 2, except the ports are different. The  $0^\circ$ – $180^\circ$  orientation is interesting for high  $\chi^*$  [Fig. 4(a)]. There are the usual five active ports, and in addition to the full stagnation point that lies off center, another full stagnation point resides at the  $Q_1$  port. In Fig. 4(b), we show the  $90^\circ$ – $270^\circ$  orientation at high  $\chi^*$ . Here, there are only three active ports, and half of the circle including port  $Q_1$  is not used. Of the three ports that are used, two serve as the inlets, and one serves as the outlet. Similarly, for high  $\chi^*$ , there are no stagnation points in the interior of the cross section with respect to  $30^\circ$ – $210^\circ$  or  $150^\circ$ – $330^\circ$  orientations at the radial locations in Fig. 4.

### B. Implementation of head-on and glancing collisions

Based on the figures above, we now define the ways of performing head-on collision. If we place the particles directed toward each other along the orientations  $60^\circ$ – $240^\circ$ ,  $120^\circ$ – $300^\circ$ , or  $0^\circ$ – $180^\circ$ , then, at high  $\chi^*$  [Fig. 5(a)], we generate a single stagnation point, and can implement a head-on collision. For convenience,  $60^\circ$ – $240^\circ$ ,  $120^\circ$ – $300^\circ$ , or  $0^\circ$ – $180^\circ$  orientation shall be now called the “axis.” For example, we show the pathway in the head-on collision in the  $60^\circ$ – $240^\circ$  orientation in a video (Video V1 in the Supplemental Material [43]). The  $30^\circ$ – $210^\circ$ ,  $90^\circ$ – $270^\circ$ , or  $150^\circ$ – $330^\circ$  configurations, called the “coaxial” configurations, do not create a stagnation point near the center of the device when the particles are a distance apart [Fig. 4(b)], but they do create a stagnation point when the particles are sufficiently close (Supplemental Video V2 [43]). However, the flow is symmetric along the axis, whereas the flow along coaxial is asymmetric. Besides, the flow along the axis always has the stagnation point in the middle of the particles, while the flow along the coaxial has a stagnation point in the corner at the beginning of the simulation, and it only moves in the center toward the end of the simulation. For the collision of Hele-Shaw drops along the coaxial where two drops come into contact before the complete evolution of the flow field, the asymmetric flow may cause an uneven distribution of the hydrodynamic force at the interface of the drops, which might lead to asymmetric deformation of the film during the coalescence time. These reasons force us to use the axial configuration instead of the coaxial configuration. For glancing collisions, instead of particles targeting themselves as in a head-on configuration, we position the origin and the target positions slightly away from the axis in concert with glancing angle  $\varphi$ , as shown in Fig. 5(b), such that the glancing collision occurs along the axis. For example, we show the pathway in the glancing collision in the  $60^\circ$ – $240^\circ$  orientation in Supplemental Video V3 [43]. In both head-on and glancing collisions, we determine the strain rate ( $G$ ) using the flow rates recorded during the experiments as the positive eigenvalue of the matrix of the rate of strain.

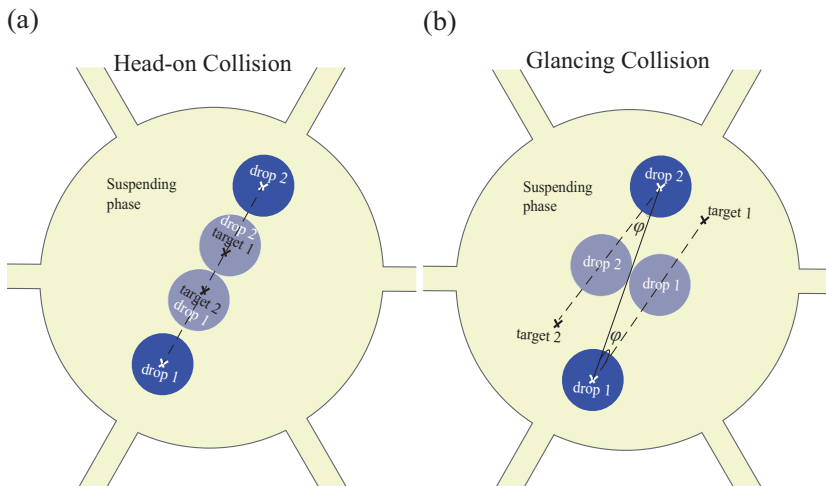


FIG. 5. Schematic of the strategy to induce head-on and glancing collision in the six-port MEFD. For head-on collision the target points are placed on the drops' centerline. For glancing collision, targets are placed within angle  $\varphi$  from the centerline.

### C. Scale $\tau^* = \chi t_{\text{loop}}$

There is a second dimensionless group governing the process:  $\tau^* = \chi t_{\text{loop}}$ . The time  $t_{\text{loop}}$  is the total time it takes for the performance of the hardware and software. To have effective control, the  $t_{\text{loop}}$  should be shorter than the inverse of the gain parameter  $1/\chi$ , i.e.,  $\tau^* = \chi t_{\text{loop}} < 1$ . This imposes an upper limit on the parameter  $\chi$ . In the experiments,  $t_{\text{loop}}$  is 80 ms; hence  $\frac{1}{\chi} > 80$  ms. Also, the value of  $\chi^* = \chi R^2 H / Q_1$  can go to around 100 in the particle manipulation and collision run. Hence, it sets a limit on characteristic timescale  $R^2 H / Q_1$  to the order of 10 s. Based on  $R = 1$  mm and  $H = 100$   $\mu\text{m}$ , the value of the maximum flow rate  $Q_1$  that we get is on the order of  $1$   $\text{mm}^3/\text{min}$ . As we shall show in Sec. IV, we approximately hit this mark, with a flow rate of  $Q_1 = 0.92$   $\text{mm}^3/\text{min}$ .

## III. HELE-SHAW DROPS AND THE CORRECTION TO THE CONTROL ALGORITHM

The principle of control algorithm that is discussed in Sec. II is independent of particle or drop size, as long as non-Brownian motion is satisfied [34]. Even though the general interest might be in studying drop collision for spherical drops [49], in this study, we have chosen to work with Hele-Shaw drops. This is because current control strategies are limited to two-dimensional (2D) manipulation of the position (see Tu *et al.* [49] for a recent exception), and any drift in the direction of the depth of the channel will impede the in-plane interaction of spherical drops. This would make it challenging to conduct experiments, as the spherical drops have to be in the same (or similar) Hele-Shaw plane to collide with each other. This means that (1) the drops have to be created in the same plane (e.g., by breaking a drop into two drops [30]), and (2) they have to be kept in the same plane. For example, effects like gravity should not be important during a collision, especially when long coalescence times are involved. This can be achieved by matching the density of suspending and dispersed phase fluids, but is restricted to a small set of systems.

The challenges associated with utilizing spherical drops are not limited to drifting. Let us consider the case when the suspending medium is opaque, but the drops are visible to bright field. Drops that are spherical make visualization significantly difficult. On the contrary, Hele-Shaw water drops in bitumen are visualized easily due to the thin film of the oil. Besides, in a microfluidic two-phase segmented flow, the Hele-Shaw drops are more likely to be generated in microfluidic chips [50], and it would be useful to study Hele-Shaw drops at varying capillary numbers.



Now, the choice of Hele-Shaw drops comes with a different set of challenges. First, we need to make the drops nonadherent to the microfluidic channel. In this study, we made the surface passive by coating (see Sec. IV for details). Second, for a constant ambient velocity field, the presence of a Hele-Shaw particle or drop of a finite radius  $R_p$  induces dipolar hydrodynamic disturbance to the flow field [37–41]. This causes it to move slower than the fluid element of the suspending medium placed at the drop’s center of mass [37–41]. We determined an analytical solution,  $\mathbf{v}_p^\infty(\mathbf{x}, \mathbf{x}_p, R_p, \mathbf{Q}/H)$ , to the flow field in the presence of a circular inset of radius  $R_p$  located at the position  $\mathbf{x}_p$ , as shown in Fig. 6(a). This leading-order modification to the flow field may not fully capture the dipolar flow perturbation and its effect on slowing down Hele-Shaw drops compared to the surrounding medium. However, the absolute value of the velocities of the drops is inconsequential in this study due to the gain parameter. If direction and order of magnitude of the velocity that is imposed on drops is the same as that of the fluid element at the positions of the drops, the conditions required for the control can be satisfied.

The first-order modification to the flow field for Hele-Shaw drops is done by calculating a solution to the Laplace equation for  $\psi_p^\infty$ , but with a circle included in the domain using a conformal mapping technique (see Supplemental Material [43], Sec. A [44]). The velocity of a particle is then  $\mathbf{v}_p^\infty = [\frac{\partial \psi_p^\infty}{\partial y}, -\frac{\partial \psi_p^\infty}{\partial x}]$ . For instance,  $\mathbf{v}_p^\infty(\mathbf{x}_A, \mathbf{x}_B, R_B, \mathbf{Q}/H)$  is the velocity of particle *A* due to a circular inset *B*, and  $\mathbf{v}_p^\infty(\mathbf{x}_B, \mathbf{x}_A, R_A, \mathbf{Q}/H)$  is the velocity of particle *B* due to a circular inset *A*, according to the method of reflections. To determine the first-order effect of the presence of a circular particle on the flow field, in Figs. 6(b) and 6(c), two particles were set to move from their initial positions ( $\mathbf{x}_{AI}$ ,  $\mathbf{x}_{BI}$ ) toward their respective targets ( $\mathbf{x}_{AT}$ ,  $\mathbf{x}_{BT}$ ). In Fig. 6(b), particles experience  $\mathbf{v}_p^\infty$  due to the presence of the other particle, but they are advanced by the flow rates that are updated based on  $\psi^\infty$ . The initial particle separation  $\delta/R$ , as indicated in Fig. 6(b), is 0.26. The value of  $\chi^*$  is much greater than 1. Estimation of the flow rates by  $\psi^\infty$  for particles that experience  $\mathbf{v}_p^\infty$  leads to deviation and overlap (11.2% of the radius) of the particles in close contact. Once  $\psi_p^\infty$  is used to update the required flow rates [Fig. 6(c)], particles experiencing flow disturbances manage to pass by each other without deviation of their center points. Note that  $\mathbf{v}_p^\infty(\mathbf{x}, \mathbf{x}_p, R_p, \mathbf{Q}/H)$  tends to  $\mathbf{v}^\infty(\mathbf{x}, \mathbf{Q}/H)$  for  $R_p \ll R$ ; hence the analytical solution is valid for point particles as well.

#### IV. EXPERIMENTAL SETUP AND PROCEDURE

To illustrate the implementation of the control, experiments were conducted by manipulating two Hele-Shaw perfluorodecalin (Sigma Aldrich, viscosity of 5 cP) drops in 500 cP silicone oil (Sigma-Aldrich). Silicone oil was pumped into the six-port MEFD through rigid PEEK tubes (0.02 inches internal diameter). As shown in Fig. 7, all six fluid reservoirs were connected to the pressure controller (Elveflow OB1, MK3) with a rise and fall response time of 20 ms. The dispersed phase liquid reservoir was also connected to a pressure controller (Marsh Bellofram). Perfluorodecalin drops were generated using a T junction by means of step emulsification [51,52] and applying the “drop-on-demand” principles [53]. It is important to have a stagnant perfluorodecalin-silicone oil interface at the T junction throughout the control to prevent the creation of new drops during the control process, which was achieved by a static pressure balance at the T junction [53]. The microfluidic channel was etched on a silicon wafer and anodically bonded to a borosilicate glass. For accurate control over pancake-shaped soft particles or drops, it was essential to prevent the wetting of the glass and silicon channel walls by the perfluorodecalin drops. To achieve this, we coated [54] the microfluidic device with 5% (w/w) polymethylpentene in hexane (Sigma-Aldrich) by applying a gas-templating method [55].

Hele-Shaw drops were controlled in the channel by the correction proposed in Sec. III. To control drops, each control loop started with the acquisition of the MEFD circle image by a camera (Teledyne Lumenera infinity3S-IURM) at 60 fps. The captured image was sent to the computer for image processing and computation of the required flow rates using MATLAB (details of the image processing as well as the schematic of the control loop are presented in the Supplemental Material [43], Sec. B). The flow rates were converted to the pressure considering  $P_m - P_0 = \mathcal{R}_m Q_m$ , where

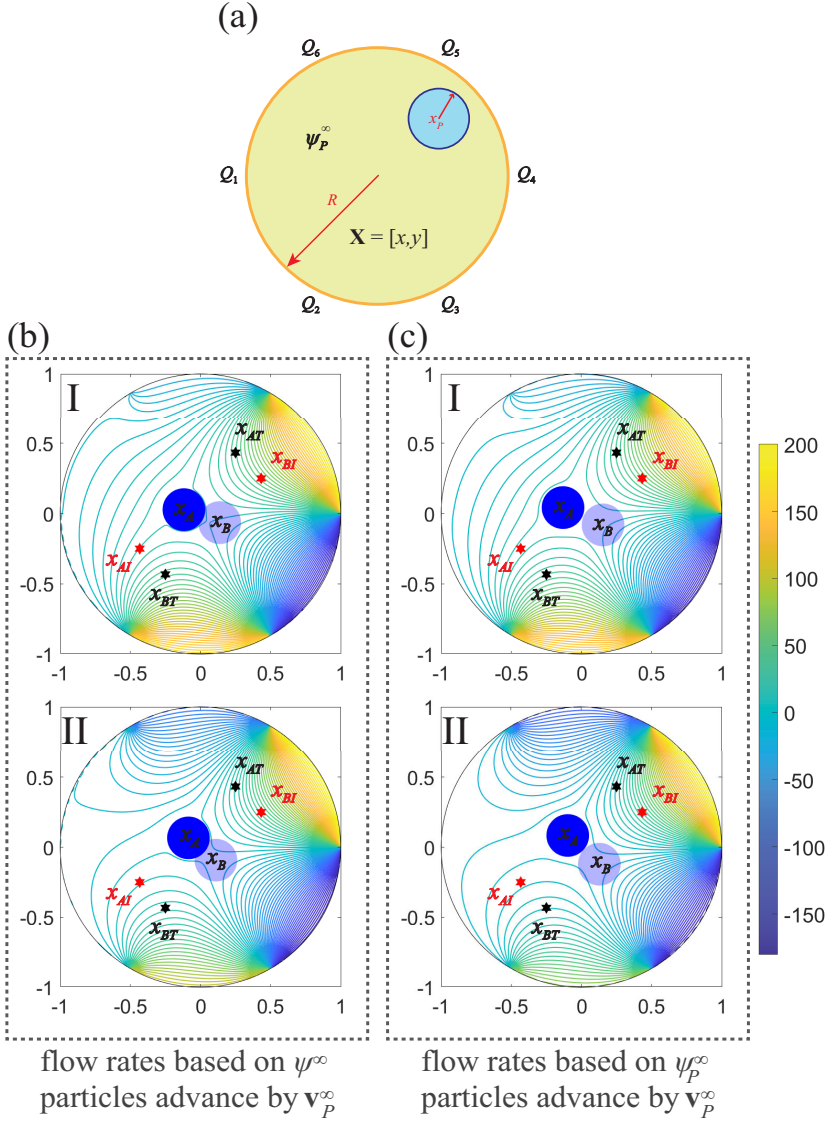


FIG. 6. (a) Geometry of the six-port MEFD circle and the flow field ( $\psi_P^\infty$ ) developed based on the presence of the circular inset at an arbitrary position,  $x_P$ . (b) The flow field evolution during the particles' manipulation from initial positions ( $x_{AI}$ ,  $x_{BI}$ ) to target positions ( $x_{AT}$ ,  $x_{BT}$ ) while the particles are advanced by  $\mathbf{v}_P^\infty$  and flow rates are updated based on the  $\psi^\infty$ . (c) The flow field evolution during the particles' manipulation from initial positions ( $x_{AI}$ ,  $x_{BI}$ ) to target positions ( $x_{AT}$ ,  $x_{BT}$ ) while the particles are advanced by  $\mathbf{v}_P^\infty$  and flow rates are updated based on  $\psi_P^\infty$ .

$P_m$  is the pressure at each fluid reservoir,  $P_0$  is the pressure at the center of the main circular channel, and  $\mathcal{R}_m$  is the hydrodynamic resistance across each side channel and its associated PEEK tubing. The pressure  $P_0$  was deduced from the incompressibility of the fluid flowing in the device, to be  $P_0 = \frac{\sum_{m=1}^6 (\frac{P_m}{\mathcal{R}_m})}{\sum_{m=1}^6 (\frac{1}{\mathcal{R}_m})}$ . In the case of equal hydrodynamic resistances in the six side channels,  $P_0$  reduces to  $P_0 = \frac{1}{6} \sum_{m=1}^6 P_m$ . For a typical collision experiment where the maximum value of  $P_m$  is 5 psi and

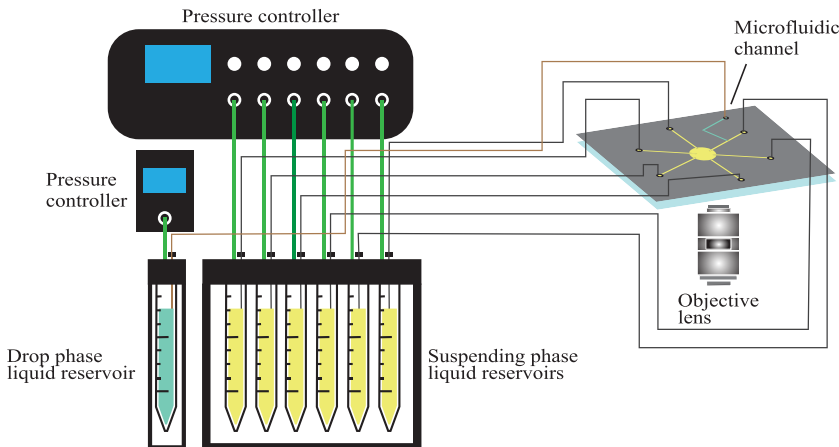


FIG. 7. The experimental setup where the six reservoirs, each delivering fluid to one of the six ports in the MEFD, are connected to the pressure controllers that are controlled using MATLAB. Yellow represents the suspending liquid medium and the blue is the dispersed phase that leads to a T junction for drop production.

$P_0$  is approximately 3.4 psi, the resistance of  $\mathcal{R}_m = 7 \times 10^{14} \text{ Pa s m}^{-3}$ , yields the maximum flow rate of  $0.92 \text{ mm}^3 \text{ min}^{-1}$ .

To perform collision experiments, after two or more drops were found in the channel, two drops needed to be brought to the axial configuration ( $60^\circ$ – $240^\circ$ ,  $120^\circ$ – $300^\circ$ , or  $0^\circ$ – $180^\circ$ ) so that the head-on or glancing collisions could be initiated, while the rest of them were flushed away. For this, the target positions were placed along the axis, and control was performed at low  $\chi^*$  or high  $\chi^*$ . Even if high  $\chi^*$  is used, as the particles near their respective target positions, as indicated in Eq. (4),  $\chi^*(\mathbf{x}_{A_T}^* - \mathbf{x}_A^*)$  and  $\chi^*(\mathbf{x}_{B_T}^* - \mathbf{x}_B^*)$  were eventually small, and particles were finally placed at their stagnation points. Pressure at all six side channels (plus the side channel connected to the dispersed phase reservoir) was set to zero, which stalled the flow and trapped drops. Thereafter, the control indicated in Fig. 5(a) for head-on collisions or Fig. 5(b) for glancing collisions was carried out.

## V. RESULTS AND DISCUSSION

### A. Demonstration of control

To demonstrate the accurate manipulation of Hele-Shaw drops, first, two drops (100 and 125  $\mu\text{m}$  radii in the device with a depth of 100  $\mu\text{m}$ ) are kept at separate but constant initial positions within 500  $\mu\text{m}$  interdrop distance for 100 s in the configuration shown in the inset of Fig. 8(a). The effects of the variation of  $\chi^*$  on the precision of control is also shown in Fig. 8(a). Both drops experience in-phase fluctuations of position ( $d$ ) with the variation of  $\chi^*$ . As they approach the targets, the prescribed velocity ( $\mathbf{v}_p^\infty$ ) that is dictated by  $\chi^*$  decreases due to a reduction in separation. Our results show that increasing  $\chi^*$  as the drops approach the target enhances the accuracy and reduces the offset. This can be seen at  $t = 95 \text{ s}$  in Fig. 8(a), where increasing the  $\chi^*$  from 50 to 100 leads to a sharp reduction of  $d$ . In Fig. 8(b), the set of drops in Fig. 8(a) was steered along the edges of a  $500 \times 500 \mu\text{m}$  square (2 mm in total) (see Supplemental Video V4 [43]). As can be seen in Fig. 8(b), the drops move in the direction of the straight line that connects the center of the drops to its target points. Figures 8(c)–8(e) show the positions of the centers of the drops during the manipulation in Fig. 8(b). While drops move monotonically, there are some deviations of the center of the drops from the straight line connecting the center to the target points. However, as shown in the Supplemental Material [43], Sec. C, these deviations are small compared to the size of the drops without any overshoots, which is a direct consequence of the matrix inversion control algorithm adopted in this

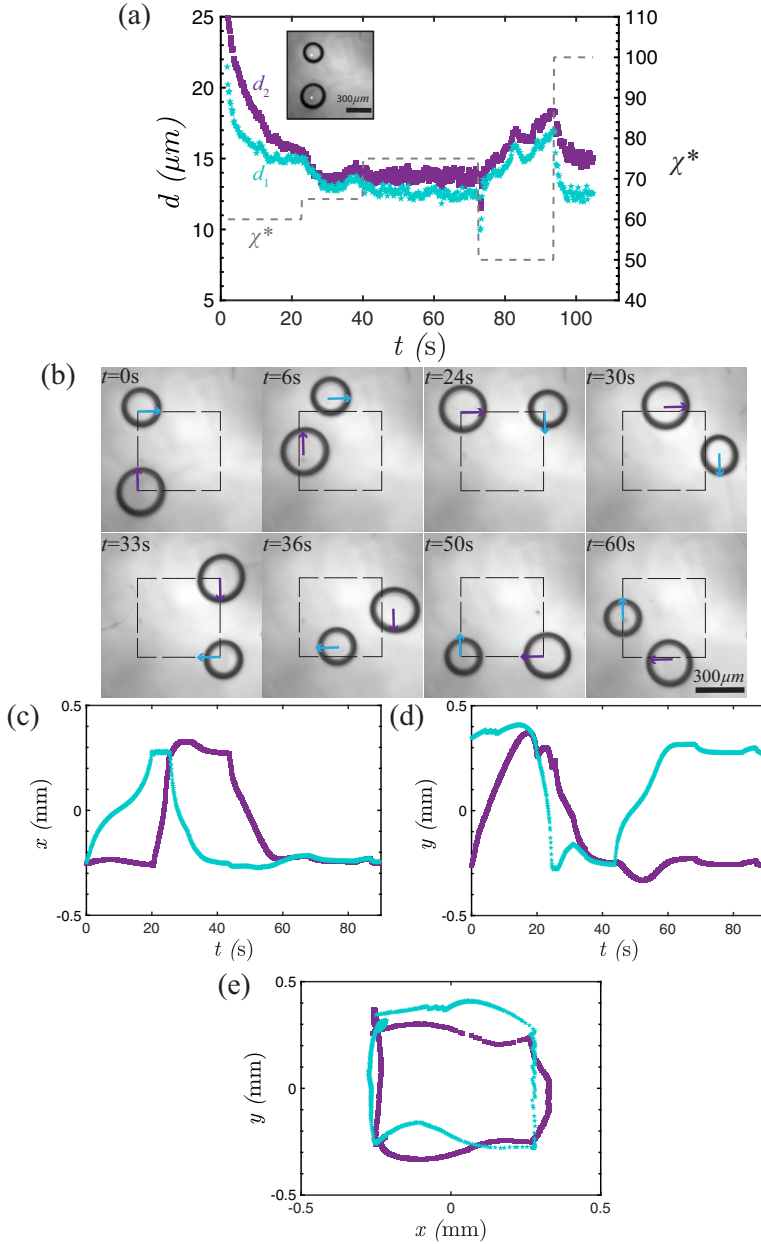


FIG. 8. Manipulation of two Hele-Shaw perfluorodecalin drops (100 and 125 microns in radii) in silicone oil. Depth of the channel ( $H$ ) is 100 microns. (a) Drops are held at a certain position for 100 s through which the distance of the center of the drops from target positions ( $d$ ), shown on the left axis, fluctuates within 5%–8% error. Values of  $\chi^*$  during the manipulation (dashed gray line) is shown on the right axis. (b) Drops are steered along a predefined path. The value of  $\chi^*$  varies in the range of 100–180 actively, with a larger  $\chi^*$  as the drops approach the target points and a smaller  $\chi^*$  while drops are far away from the targets. The total loop time for this case is 84 ms. When the two drops reach within a certain distance from the target points (20 microns in this experiment), the target points are updated, and the drops are steered toward the next set of target points. (c,d) The variation of the centers of the drops in the  $x$  and  $y$  directions, with time, and (e) the trajectories of both the centers of the drops along the predefined path in (b).

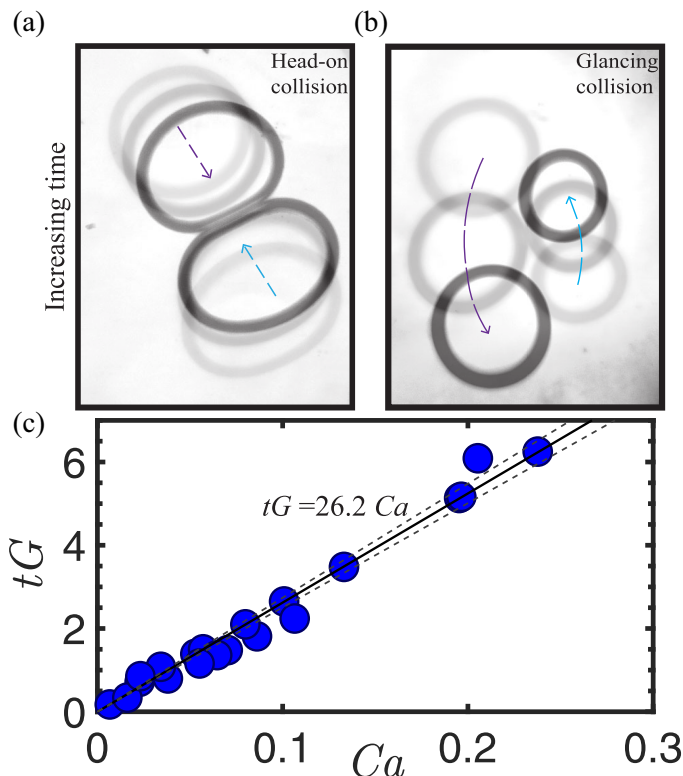


FIG. 9. Demonstration of two Hele-Shaw perfluorodecalin drops suspended in silicone oil undergoing (a) head-on and (b) glancing configurations. The time taken for glancing and head-on collisions is 13 and 6 s, respectively. (c) Dimensionless drainage time ( $tG$ ) as a function of capillary number ( $Ca$ ) number for head-on collision of the Hele-Shaw ( $R_p = 110 \pm 13 \mu\text{m}$ ) perfluorodecalin drops in silicone oil; the drainage time scales as  $t \sim \frac{\lambda\mu R_p}{\gamma} \frac{\sqrt{H}}{\sqrt{h_f}}$ , where  $\lambda$  is the viscosity ratio,  $\mu$  is the viscosity of suspending phase,  $\gamma$  is the interfacial tension, and  $h_f$  is the final film thickness. The equation of the linear fit is shown on the graph with 95% confidence bounds (25.06, 27.39) shown with dashed lines.

work [33]. It takes 60 s for the drops to complete the entire trajectory, covering a length that is an order of magnitude larger than the size of the drops. The average velocity of Hele-Shaw drops in our experiments is  $30 \mu\text{m s}^{-1}$ . The average velocity of drops that is theoretically determined as  $\mathbf{v}_P^\infty = [\frac{\partial\psi_P^\infty}{\partial y}, -\frac{\partial\psi_P^\infty}{\partial x}]$  by reconstruction of the flow field ( $\psi_P^\infty$ ) using the pressures that were collected during the experiments, is shown in the Supplemental Material [43], Sec. C (Fig. S4).

### B. Demonstration of head-on and glancing collisions

Figures 9(a) and 9(b) demonstrate the collision of a pair of Hele-Shaw drops undergoing head-on and glancing collisions, respectively, using the control strategy explained in Sec. II B and Fig. 5 (see the Supplemental Videos V5 and V6 [43]). The value of  $\chi^*$  was set to 100 in the collision experiments, so while drops are moving toward each other, a single stagnation point forms in between them (Sec. II B). As the strain rate  $G$  is a function of position in the correction for Hele-Shaw drops, its value is slightly different at the center of each particle, so the average value of  $G$  was considered in analyzing the collision experiments. In a head-on collision [Fig. 9(a)], once drops come into contact, a constant hydrodynamic force pushes the drops against each other indefinitely until the drops coalesce within a drainage time ( $t$ ). The drops are not able to separate

away due to the control over both drops (see Sec. VI for more details). We chose  $t = 0$  corresponding to the moment where the distance between the two Hele-Shaw drops was  $R_{p_1} + R_{p_2}$ , the radii of the two drops. On the other hand, in a glancing collision [Fig. 9(b)], the two drops collide and rotate until the point where the hydrodynamic force changes the sign, and the drops separate away [30].

### C. Drainage time measurement in a head-on collision between drops

We have measured the hydrodynamic drainage time for two Hele-Shaw drops that come into contact through head-on collision in the extensional flow. Figure 9(c) shows the dimensionless drainage time ( $tG$ ) variation with Ca number ( $\text{Ca} = \frac{4\mu GR^3}{\gamma H^2}$ ) [20], where  $G$  is the strain rate of the flow,  $\mu$  is the viscosity of the suspending fluid, and  $\gamma$  is the interfacial tension (IFT) of the perfluorodecalin-silicone oil interface that is measured, using an in-house four-port MEFD, to be  $1.4 \text{ mN m}^{-1}$ . The details of the calculations of the  $\gamma$  measurements are discussed in the Supplemental Material [43], Sec. C [45]. The drainage time was measured from  $t = 0$  until the instant two drops merge. This is an example of the hydrodynamic drainage time being measured experimentally at a mobile interface and in the limits of Hele-Shaw motion for two drops. The linearity of the  $tG$ -Ca curve in Fig. 9(c) suggests the independence of the drainage time from the strain rate in head-on collision. The theory supports this result (derivation given in the Supplemental Material [43], Sec. D):

$$t \sim \frac{\lambda \mu R_P}{\gamma} \frac{\sqrt{H}}{\sqrt{h_f}}. \quad (6)$$

Here,  $\lambda$  is the dispersed to suspending phase viscosity ratio and  $h_f$  is the final height of the film. The cause for this is as follows. Continuity requires that the rate of volume decrease is equal to the drainage velocity multiplied by the cross-sectional coordinates. It is known theoretically that for unconfined drops, the rate of the volume decrease is the square of the film radius, but the velocity term is directly proportional to the film radius; hence the drainage decrease rate is inversely proportional to the film radius [30,46,47]. However, for the Hele-Shaw drops, the film radius features linearly on both sides of the continuity equation, and its effect on the strain rate vanishes [48].

## VI. DISCUSSION

A few comments about the analytical method of collision in the six-port device are in order here. The flow rate matrix ( $\mathbf{Q}$ ) is rendered dimensionless using the positive flow rate at the first port ( $Q_1$ ). This nondimensionalization can be performed based on the flow at any of the six ports, and by assigning a positive or negative flow to the port in question, so for a single value of  $\chi^*$ , there exist 12 different solutions to the topology. However, as far as the axes and coaxes are concerned, the head-on and glancing collision will appear to be the same, as shown in Figs. 2 and 4.

In order for the particles to get from one position to another, it is said that particle encounters are discouraged, as that leads to a high dissipation rate [17,32,33]. This can be done via MPC by employing  $\beta$ , the regularizer for flow rate [32,33]. In this study, for the initial manipulation to get particles to the axis, we use, not MPC, but our analytical algorithm at low  $\chi^*$  or at high  $\chi^*$ , as indicated in Sec. IV. If the flow rates are unusually large, which are detected by the pressure drops, and if we are not concerned about the strain rate, which is valid in the initial manipulation, we can always divide the flow rate by a factor to keep the flow rate in control. But after the setting of the particles on the axis is done, the idea is to create an encounter or a collision; therefore, we cannot invoke the minimum dissipation idea. Moreover, a single stagnation point is generated in the interior of the channel for head-on or and glancing collisions along the axis in the limit  $\chi^* \gg 1$  using the analytical method. These are created by flow through five ports at  $\chi^* \gg 1$ , not six: the extra degree of freedom is lost (Sec. II). If a collision is to be performed at a controlled strain rate, which is modulated by the flow rate, there is only one option of flow rates along the axis according to the analytical solution, not multiple.

The half stagnation points generated in the  $N$ -port device are of particular interest to us, in the light of the idea that  $2N + 1$  ports are required to control  $N$  particles [17]. They occur in our four-



port device as well—one can have a single stagnation point, or two half stagnation points. In the five-port device, a single stagnation point and a half stagnation point, or three half stagnation points could exist in the device. In the six-port device, two stagnation points, or one stagnation point and two half stagnation points, or four half stagnation points could persist. One can have a half stagnation point in a three-port device as well, and trap a particle [17]. Our preliminary investigations also indicate that in a five-port device, collision may also be carried out, as indicated by Shenoy *et al.* [33]. This is left to future work.

We have used the Hele-Shaw microfluidic channel in this work. In a Hele-Shaw channel, the width is much greater than the depth. Hence, vorticity in the Hele-Shaw depth direction is negligible, and rotational flows are barely permitted; one has to resort to extensional flows only. For example, in a four-port MEFD, one needs to resort to extensional alignment of a particle; there is no rotational help to assist motion. Therefore, short term head-on collision is possible with a four-port device. On the original, computer controlled four-roll mill [27], two drops were brought into head-on collision in an extensional flow, but because of the rotation possible in the four-roll mill, the drops could be kept infinitely long in the configuration. However, on a microfluidic, Hele-Shaw, four-roll mill, we cannot do head-on collisions of two drops for a relatively long period of time, as there is no rotational help. With a six-port MEFD, however, the two drops are controlled by separate target points (Fig. 5) and, therefore, the head-on collision can be performed on the two drops as long as the liquid lasts in the pressure reservoirs.

The total loop time in our experiments is approximately 80 ms with the following time breakdown:

- (1) grabbing the image by camera ( $\sim 17$  ms),
- (2) performing image processing ( $\sim 45$  ms),
- (3) computing of the flow rates and pressures through the analytical solution ( $\sim 13$  ms), and
- (4) communicating with pressure controllers ( $\sim 5$  ms).

The comparable total loop time corresponding to MPC, according to Ref. [32], is 33 ms. This is obviously shorter than our 80 ms timescale, but remember that the analysis was done using LABVIEW, an advanced data analysis and control software program. We have done the computation and analysis using an interpreted language, MATLAB, which is considerably slower. If LABVIEW is used, our computations will be much faster.

## VII. CONCLUSIONS

In the current paper, manipulation of a pair of particles along the desired trajectories is demonstrated by employing the matrix inversion method to determine the required flow rates in a six-port MEFD. In past practices, the use of the matrix inversion method to determine the flow rates has been discouraged as it leads to a high dissipation rate for the trajectories that involve encounter of particles. However, this paper shows that the matrix inversion method can effectively steer particles toward their respective targets by using a single control parameter,  $\chi^*$ .  $\chi^*$  is the characteristic timescale required to sweep the volume of the MEFD circle relative to the timescale of control. Changing the value of  $\chi^*$  from zero to its maximum, which is determined based on the loop time, leads to variation in the topology of the flow field from two stagnation point flow ( $\chi^* \ll 1$ ) to the linear extensional flow ( $\chi^* \gg 1$ ). The system was used to design and carry out systematic head-on and glancing collision between a pair of Hele-Shaw drops. To account for the hydrodynamic interaction between the Hele-Shaw drops, a correction was calculated by eliminating a circular drop in the six-port device by using the conformal mapping technique.

For confined drops undergoing the head-on collision, drainage time in the film was insensitive to the strain rate, whereas for unconfined drops, the drainage rates have shown a strain rate power of  $\frac{1}{3}$  [30,46]. This was explained on the basis of the continuity equation. The film radius corresponding to the dimpled film is the primary quantity which affects the capillary number, and continuity requires that the film radius be canceled out, hence the result.

There are several implications of this work, and we name two here. First, the coalescence of two Hele-Shaw drops will require a much longer investigation. There are several variables to be explored (viscosity ratio, radius of the drop, channel depth and width, etc.), and these will be investigated to quantify drainage time in head-on as well as glancing collisions. Second, coalescence of drops of two different phases in the third suspending phase, which leads to the formation of compound drops [56] (from core shell to Janus) can be performed using the methodology explained here.

#### ACKNOWLEDGMENTS

We acknowledge the funding support from Syncrude Canada Ltd. and Natural Science and Engineering Research Council of Canada under Collaborative and Research Development Grant No. CRDPJ 514675-17. A. Ramachandran acknowledges Canada Research Chair (File No. 950-231567).

- 
- [1] S. Zhang, E. Y. Scott, J. Singh, Y. Chen, Y. Zhang, M. Elsayed, M. D. Chamberlain, N. Shakiba, K. Adams, S. Yu, C. M. Morshead, P. W. Zandstra, and A. R. Wheeler, The optoelectronic microrobot: A versatile toolbox for micromanipulation, *Proc. Natl. Acad. Sci. USA* **116**, 14823 (2019).
  - [2] G. Bolognesi, M. S. Friddin, A. Salehi-Reyhani, N. E. Barlow, N. J. Brooks, O. Ces, and Y. Elani, Sculpting and fusing biomimetic vesicle networks using optical tweezers, *Nat. Commun.* **9**, 1882 (2018).
  - [3] D. G. Grier, A revolution in optical manipulation, *Nature (London)* **424**, 810 (2003).
  - [4] C. Gosse and V. Croquette, Magnetic tweezers: Micromanipulation and force measurement at the molecular level, *Biophys. J.* **82**, 3314 (2002).
  - [5] R. Sarkar and V. V. A. Rybenkov, Guide to magnetic tweezers and their applications, *Front. Phys.* **4**, 48 (2016).
  - [6] A. Ozcelik, J. Rufo, F. Guo, Y. Gu, P. Li, J. Lata, and T. J. Huang, Acoustic tweezers for the life sciences, *Nat. Methods* **15**, 1021 (2018).
  - [7] A. E. Cohen and W. E. Moerner, Method for trapping and manipulating nanoscale objects in solution, *Appl. Phys. Lett.* **86**, 093109 (2005).
  - [8] R. Probst and B. Shapiro, Three-dimensional electrokinetic tweezing: Device design, modeling, and control algorithms, *J. Micromech. Microeng.* **21**, 027004 (2011).
  - [9] A. Atajanov, A. Zhanov, and S. Yang, Sorting and manipulation of biological cells and the prospects for using optical forces, *Micro and Nano Syst. Lett.* **6**, 2 (2018).
  - [10] S. L. Poliachik, W. L. Chandler, P. D. Mourad, R. J. Ollos, and L. A. Crum, Activation, aggregation, and adhesion of platelets exposed to high-intensity focused ultrasound, *Ultrasound Med. Biol.* **27**, 10 (2001).
  - [11] G. I. Taylor, The formation of emulsions in definable fields of flow, *Proc. R. Soc. Lond. A* **146**, 501 (1934).
  - [12] H. P. Grace, Dispersion phenomena in high viscosity immiscible fluid systems and application of static mixers as dispersion devices in such systems, *Chem. Eng. Commun.* **14**, 225 (1982).
  - [13] B. J. Bentley and L. G. Leal, A computer-controlled four-roll mill for investigations of particle and drop dynamics in two-dimensional linear shear flows, *J. Fluid Mech.* **167**, 219 (1986).
  - [14] S. D. Hudson, F. R. Phelan, M. D. Handler, J. T. Cabral, K. B. Migler, and E. J. Amis, Microfluidic analog of the four-roll mill, *Appl. Phys. Lett.* **85**, 335 (2004).
  - [15] J. S. Lee, R. Dylla-Spears, N. P. Tecelemarian, and S. J. Muller, Microfluidic four-roll mill for all flow types, *Appl. Phys. Lett.* **90**, 074103 (2007).
  - [16] M. Tanyeri, E. M. Johnson-Chavarría, and C. M. Schroeder, Hydrodynamic trap for single particles and cells, *Appl. Phys. Lett.* **96**, 224101 (2010).
  - [17] T. M. Schneider, S. Mandre, and M. P. Brenner, Algorithm for a Microfluidic Assembly Line, *Phys. Rev. Lett.* **106**, 094503 (2011).

- [18] M. Tanyeri, M. Ranka, N. Sittipolkul, and C. M. Schroeder, A microfluidic-based hydrodynamic trap: Design and implementation, *Lab Chip* **11**, 1786 (2011).
- [19] M. Tanyeri and C. M. Schroeder, Manipulation and confinement of single particles using fluid flow, *Nano Lett.* **13**, 2357 (2013).
- [20] A. H. Motagamwala, A microfluidic, extensional flow device for manipulating soft particles, M.Sc. thesis, University of Toronto, 2013.
- [21] S. Narayan, D. B. Moravec, A. J. Dallas, and C. S. Dutcher, Droplet shape relaxation in a four-channel microfluidic hydrodynamic trap, *Phys. Rev. Fluids* **5**, 113603 (2020).
- [22] R. G. Cox, The deformation of a drop in a general time-dependent fluid flow, *J. Fluid Mech.* **37**, 601 (1969).
- [23] S. J. Haward, M. S. N. Oliveira, M. A. Alves, and G. H. McKinley, Optimized Cross-Slot Flow Geometry for Microfluidic Extensional Rheometry, *Phys. Rev. Lett.* **109**, 128301 (2012).
- [24] F. Del Giudice, S. J. Haward, and A. Q. Shen, Relaxation time of dilute polymer solutions: A microfluidic approach, *J. Rheol.* **61**, 327 (2017).
- [25] A. R. Metcalf, S. Narayan, and C. S. Dutcher, A review of microfluidic concepts and applications for atmospheric aerosol science, *Aerosol Sci. Technol.* **52**, 310 (2018).
- [26] Y. T. Hu, D. J. Pine, and L. G. Leal, Drop deformation, breakup, and coalescence with compatibilizer, *Phys. Fluids* **12**, 484 (2000).
- [27] H. Yang, C. C. Park, Y. T. Hu, and L. G. Leal, The coalescence of two equal-sized drops in a two-dimensional linear flow, *Phys. Fluids* **13**, 1087 (2001).
- [28] C. C. Park, F. Baldessari, and L. G. Leal, Study of molecular weight effects on coalescence: Interface slip layer, *J. Rheol.* **47**, 911 (2003).
- [29] J. W. Ha, Y. Yoon, and L. G. Leal, The effect of compatibilizer on the coalescence of two drops in flow, *Phys. Fluids* **15**, 849 (2003).
- [30] L. G. Leal, Flow induced coalescence of drops in a viscous fluid, *Phys. Fluids* **16**, 1833 (2004).
- [31] A. S. Hsu, A. Roy, L. G. Leal, Drop-size effects on coalescence of two equal-sized drops in a head-on collision, *J. Rheol.* **52**, 1291 (2008).
- [32] A. Shenoy, C. V. Rao, and C. M. Schroeder, Stokes trap for multiplexed particle manipulation and assembly using fluidics, *Proc. Natl. Acad. Sci. USA* **113**, 3976 (2016).
- [33] A. Shenoy, D. Kumar, S. Hilgenfeldt, and C. M. Schroeder, Flow Topology During Multiplexed Particle Manipulation Using a Stokes Trap, *Phys. Rev. Appl.* **12**, 054010 (2019).
- [34] J. Boyd, G. Hepner, M. Ujhazy, S. Bliss, and M. Tanyeri, Dual hydrodynamic trap based on coupled stagnation point flows, *Phys. Fluids* **35**, 062001 (2023).
- [35] D. Kumar, A microfluidic device for producing controlled collisions between two soft particles, M.Sc. thesis, University of Toronto, 2016.
- [36] S. Narayan, I. Makhnenko, D. B. Moravec, B. G. Hauser, A. J. Dallas, and C. S. Dutcher, Insights into the microscale coalescence behavior of surfactant-stabilized droplets using a microfluidic hydrodynamic trap, *Langmuir* **36**, 9827 (2020).
- [37] T. Beatus, T. Tlusty, and R. Bar-Ziv, Phonons in a one-dimensional microfluidic crystal, *Nat. Phys.* **2**, 743 (2006).
- [38] T. Beatus, T. Tlusty, and R. Bar-Ziv, Burgers Shock Waves and Sound in a 2D Microfluidic Droplets Ensemble, *Phys. Rev. Lett.* **103**, 114502 (2009).
- [39] T. Beatus, T. Tlusty, and R. Bar-Ziv, The physics of 2D microfluidic droplet ensembles, *Phys. Rep.* **516**, 103 (2012).
- [40] I. Shani, T. Beatus, R. H. Bar-Ziv, and T. Tlusty, Long-range orientational order in two-dimensional microfluidic dipoles, *Nat. Phys.* **10**, 140 (2014).
- [41] L. Zhu and F. Gallaire, A pancake droplet translating in a Hele-Shaw cell: Lubrication film and flow field, *J. Fluid Mech.* **798**, 955 (2016).
- [42] L. G. Leal, *Advanced Transport Phenomena*, Cambridge Series in Chemical Engineering, Vol. 7 (Cambridge University Press, Cambridge, 2007), p. 576.

- [43] See Supplemental Material at <http://link.aps.org/supplemental/10.1103/PhysRevFluids.8.084201> for the derivation of the analytical solution of the flow field [44], details on image processing and experiments, IFT measurements [20,45], strain rate calculations, and film drainage scaling analyses [46–48].
- [44] M. D. Greenberg, *Advanced Engineering Mathematics* (Prentice Hall, Englewood Cliffs, NJ, 1998).
- [45] S. Goel, N. Joshi, M. S. Uddin, S. Ng, E. Acosta, and A. Ramachandran, Interfacial tension of the water-diluted bitumen interface at high bitumen concentrations measured using a microfluidic technique, *Langmuir* **35**, 15710 (2019).
- [46] A. Ramachandran and L. G. Leal, Effect of interfacial slip on the thin film drainage time for two equal-sized, surfactant-free drops undergoing a head-on collision: A scaling analysis, *Phys. Rev. Fluids* **1**, 064204 (2016).
- [47] S. Goel and A. Ramachandran, The suppression of droplet-droplet coalescence in a sheared yield stress fluid, *J. Colloid Interface Sci.* **492**, 199 (2017).
- [48] S. Goel, S. Ng, E. Acosta, and A. Ramachandran, The roles of contact time and contact pressure on the coalescence of water droplets suspended in concentrated bitumen solutions, *Fuel* **223**, 486 (2018).
- [49] M. Q. Tu, H. V. Nguyen, E. Foley, M. I. Jacobs, and C. M. Schroeder, 3D manipulation and dynamics of soft materials in 3D flows, *J. Rheol.* **67**, 877 (2023).
- [50] D. Dendukuri, S. S. Gu, D. C. Pregibon, T. A. Hatton, and P. S. Doyle, Stop-flow lithography in a microfluidic device, *Lab Chip* **7**, 818 (2007).
- [51] M. L. Eggersdorfer, H. Seybold, A. Ofner, D. A. Weitz, and A. R. Studart, Wetting controls of droplet formation in step emulsification, *Proc. Natl. Acad. Sci. USA* **115**, 9479 (2018).
- [52] R. Dangla, E. Fradet, Y. Lopez, and C. N. Baroud, The physical mechanisms of step emulsification, *J. Phys. D: Appl. Phys.* **46**, 114003 (2013).
- [53] A. J. Teo, K. H. Li, N. T. Nguyen, W. Guo, N. Heere, H. D. Xi, C. W. Tsao, W. Li, and S. H. Tan, Negative pressure induced droplet generation in a microfluidic flow-focusing device, *Anal. Chem.* **89**, 4387 (2017).
- [54] L. K. Fiddes, N. Raz, S. Srigunapalan, E. Tumarkan, C. A. Simmons, A. R. Wheeler, and E. Kumacheva, A circular cross-section PDMS microfluidics system for replication of cardiovascular flow conditions, *Biomaterials* **31**, 3459 (2010).
- [55] D. Daniel, J. V. Timonen, R. Li, S. J. Velling, and J. Aizenberg, Oleoplaning droplets on lubricated surfaces, *Nat. Phys.* **13**, 1020 (2017).
- [56] N. Blanken, M. S. Saleem, M. J. Thoraval, and C. Antonini, Impact of compound drops: A perspective, *Curr. Opin. Colloid Interface Sci.* **51**, 101389 (2021).